P-BAND SAR TOMOGRAPHY OF THE REMNINGSTORP FOREST SITE

Stefano Tebaldini

Politecnico di Milano

***Abstract*—This paper is devoted to reporting the results of the tomographic analysis of the forest site of Remningstorp, Sweden. The analysis has been based on a data-set of 9 P-Band, fully polarimetric SAR images acquired by the DLR airborne system E-SAR. The acquisition campaign has been carried out in Spring 2007, in the framework of the ESA project BioSAR, aiming at the investigation of radar signatures of boreal forests. Thanks to the availability of multi-baseline and multipolarimetric data, both the polarimetric signature and the vertical structure of the Remningstorp forest have been analyzed. As a result, the following analyses will be presented: 1) Analysis of the polarimetric signature; 2) Single and multi-polarimetric spectral analysis of the forest vertical structure; 3) Parametric estimation of the forest vertical structure; 4) Separation of the polarimetric signatures associated the ground and canopy. As a result, different kinds of arguments will be presented that indicate that the Radar signature of the Remningstorp forest at P-Band is mainly due to contributions from the ground, whereas contributions from the canopy have turned out to methodically weaker, even in the HV channel. From a physical point of view, this result is consistent with the hypothesis of double bounce contributions due to both trunk-ground and canopy-ground interactions, eventually perturbed by the presence of understory, trunk and ground roughness, or by small oscillations in the local topography.**

I. INTRODUCTION

In recent years the exploitation of multi-baseline SAR data for conducting tomographic analysis has been the object of a growing interest. Due to the capability of tomographic techniques to resolve multiple targets within the same slant range, azimuth resolution cell, SAR Tomography (T-SAR) constitutes a unique tool for conducting RADAR analysis over scene characterized by a complex vertical structure, such as urban and forested areas. In its most basic formulation, the aim of T-SAR is to retrieve the vertical distribution of the backscattered power within the system resolution cell, basing on the availability of multibaseline acquisitions. A possible solution to do this is to exploit super-resolution techniques developed in the Direction of Arrival (DOA) framework, such as Capon adaptive filtering, MUSIC, SVD analysis, and others. In the framework of T-SAR, such techniques have been applied in a number of works, among which [1], [2], [3]. The main limitation of super-resolution techniques derives from the assumption that the scene is constituted by a finite number of point-like scatterers, which hinders their application in the analysis of scenarios characterized by the presence of distributed targets. For this reason, super-resolution techniques seem to be mainly suited for the tomographic characterization of urban areas. A different solution may be found in the works by *Fornaro et al.*, [4], and *Cloude*, [5], [6], where super-resolution is achieved by exploiting a priori information about target location, such as ground topography and canopy top height [6]. Polarimetric SAR Interferometry (PolInSAR) due to *Cloude and Papathanassiou*, adopts a different philosophy, in the sense that the scene analysis is carried out through the inversion of a physical model of forested areas [7], [8]. In such model, commonly referred to as Random Volume over Ground (RVoG) model, the vegetation layer is modeled as a layer of a certain thickness containing a volume with randomly oriented particles, located over a ground scatterer. As shown by the authors, the inversion of the RVoG model may be performed provided that two fully polarimetric SAR images, acquired from different points of view, of the scene are available. An advantage that results from the exploitation of a physical model is that the imaged scene is characterized in terms of the model parameters, such as, for example, ground and canopy elevation, thus allowing a direct interpretation of the results at vast scales.

In this paper it is considered the problem of the estimation of the vertical structure of forested areas through multiple SAR observations, with reference to either single or multi-polarimetric acquisitions. The aim is to pose the tomographic problem in such a way as to merge the super-resolution capabilities that DOA techniques can provide by exploiting the availability of multiple baselines with the direct estimation of forest parameters provided by the adoption of a physical model. On this basis, T-SAR will be formulated as the problem of detecting the number of targets within the slant range, azimuth resolution cell, estimating the parameters that describe their physical structure and evaluating the associated backscattered powers.

II. SINGLE CHANNEL TOMOGRAPHY

Many excellent works have been done on modeling radar backscattering for forested areas, see for example [9]. After these works, within this paper we will assume radar backscattering from forested areas to be constituted by the following measurable (at least theoretically) scattering mechanisms: backscatter from the canopy, backscatter from the ground, double bounce scattering due to trunk-ground interactions, double bounce scattering due to canopy-ground interactions. In the case where single polarimetric, multi baseline acquisitions are available, the element of diversity among these mechanisms is represented by their spatial structure. Trunk-ground interactions give rise to a point-like scattering mechanism

Proc. of '4th Int. Workshop on Science and Applications of SAR Polarimetry and Polarimetric Interferometry – PolInSAR 2009', 26–30 January 2009, Frascati, Italy (ESA SP-668, April 2009)

whose phase center is ground locked. Ground backscatter and canopy-ground interactions give rise to a distributed, ground locked, scattering mechanism. Canopy backscatter gives rise to a distributed scattering mechanism whose phase center is located above the ground, depending on canopy height. The problem is now how to properly represent the properties of all of these scattering mechanisms. Consider the case of a single polarimetric, multi-baseline data-set, represented by N Single Look Complex (SLC) SAR images, properly co-registered and phase flattened [10]. Let y_n denote a complex valued pixel in the $n-th$ image, the dependence on the slant range, azimuth location being made implicit in order to simplify the notation. Dealing with natural scenarios, it is sensible to assume that the target signature changes randomly from one pixel to another, either in the case of distributed or point-like targets. For this reason, the data will be assumed to be a realization of a zero-mean complex process. Accordingly, it follows that a unified mathematical treatment of all the scattering mechanisms described above may be provided by embedding the physics of the targets in the second order moments of the data, represented by the expected value of the interferograms. Under the hypothesis of statistical independence among the different scattering mechanisms, the expected value of the $nm-th$ interferogram may be expressed as:

$$E\left[y_n y_m^*\right] = \sum_{k=1}^{K} \sigma_k^2 \gamma_{nm}^{(k)} \exp\left(j\varphi_{nm}^{(k)}\right) + \sigma_w^2 \delta_{n-m} \qquad (1)$$

where: K is the total number of targets in the resolution cell; σ_k^2 is the backscattered power associated to the $k-th$ target; $\gamma_{nm}^{(k)}$ is the coherence induced by the spatial structure (i.e.: point-like, superficial, or volumetric) of the $k-th$ target in the $nm-th$ interferogram [11]; $\varphi_{nm}^{(k)}$ is the phase due to the $k-th$ target in the $nm-th$ interferogram [11], [10]; σ_w^2 accounts for a generic white noise contribution, which can arise from either thermal noise or clutter. After (1), the expression of the data covariance matrix is given by:

$$E\left[\mathbf{y}_{MB}\mathbf{y}_{MB}^H\right] \stackrel{def}{=} \mathbf{R} = \sum_{k=1}^{K+1} \sigma_k^2 \mathbf{R}_k \qquad (2)$$
$$\sigma_{K+1}^2 = \sigma_w^2; \qquad \mathbf{R}_{K+1} = \mathbf{I}_N$$

where $\mathbf{y}_{MB}$ is the stack of the multi-baseline data, $\{y_n\}_{n=0}^{N-1}$, at a certain slant range, azimuth location, $\mathbf{I}_N$ is the $N \times N$ identity matrix, and the superscript ^{H} indicates Hermitian transposition. The role of each matrix $\mathbf{R}_k$ in (2) is to account for the spatial structure of the $k-th$ target in the resolution cell. According to this interpretations, such matrices will be hereinafter referred to as *structure matrices*.

A. Parametrization of the structure matrices

A difficulty in the parametrization of the structure matrices is related to the choice of models to represent the targets. For the parametrization to be effective such models should include as few unknowns as possible, and should be capable of representing a wide range of targets. Consider the case of a point-like scatterer located at an elevation z with respect to a reference DEM. The expected value of the $nm-th$ interferogram is given by:

$$E\left[y_n y_m^*\right]_{(ps)} = \sigma_{(ps)}^2 \exp\left(j\frac{4\pi}{\lambda r}\frac{b_m - b_n}{\sin\theta} z\right) \qquad (3)$$

where: λ is the carrier wavelength; r is the slant range location of the target; θ is the look angle; b_n is the value of the normal baseline for the $n-th$ image; and $\sigma_{(ps)}^2$ is the backscattered power associated to the scatterer. In the case of a superficial scattering mechanism, instead, the expected value of the interferogram is given by:

$$E\left[y_n y_m^*\right]_{(sup)} = \sigma_{(sup)}^2 \gamma_{nm}^{(sup)} \exp\left(j\frac{4\pi}{\lambda r}\frac{b_m - b_n}{\sin\theta} z\right) \qquad (4)$$

where $\gamma_{nm}^{(sup)}$ is the coherence loss induced by a superficial scattering mechanism [12], [11] and $\sigma_{(sup)}^2$ is the backscattered power associated to the superficial scattering mechanism. The case of volumetric scattering requires a more careful treatment. Let $\sigma_s^2(z)$ represents the variation of the backscattered power $\sigma_s^2(z)$ along the vertical direction. By approximating the volume into which the scattering occurs as the superposition of an infinite number of planes, parallel to the ground and displaced along the vertical direction, after [11] it is straightforward to show that:

$$E\left[y_n y_m^*\right]_{(vol)} \simeq \gamma_{nm}^{(sup)} \int \sigma_s^2(z) \exp\left(j\frac{4\pi}{\lambda r}\frac{b_m - b_n}{\sin\theta} z\right) dz \qquad (5)$$

Accordingly, the problem is now how to characterize the vertical distribution of the backscattered power, $\sigma_s^2(z)$. Within this paper, it will be assumed that $\sigma_s^2(z)$ is symmetric about some point z along the vertical direction, which may be thought of as the phase center of the volumetric scatterer. Under this assumption (5) simplifies to:

$$E\left[y_n y_m^*\right]_{(vol)} = \sigma_{(vol)}^2 \gamma_{0nm}^{(sup)} \gamma_{nm}^{(vol)} \exp\left(j\frac{4\pi}{\lambda r}\frac{b_m - b_n}{\sin\theta} z\right) \qquad (6)$$

where $\gamma_{nm}^{(vol)}$ is a real number representing the coherence loss induced by the volumetric distribution of the target and $\sigma_{(vol)}^2$ is the total backscattered power associated to the volumetric scattering mechanism. From a physical point of view, the assumption of symmetry for $\sigma_s^2(z)$ is justified provided that the scattered wave originating from the vegetation layer may be described through the first Born approximation, neglecting extinction phenomena. Such hypothesis can be retained in the case of a significant penetration of the impinging wave into the vegetation and in absence of relevant multiple scattering mechanisms within the vegetation layer. If these conditions are fulfilled, it follows that $\sigma_s^2(z)$ is proportional to the vegetation density, which can be retained, as a first approximation, to be symmetric along the vertical direction. Accordingly, in all cases the phase due to the $k-th$ target in the $nm-th$ interferogram can be represented by a single parameter through:

$$\varphi_{nm}^{(k)} = \angle\left\{\mathbf{R}_k\right\}_{nm} = \frac{4\pi}{\lambda r}\frac{b_m - b_n}{\sin\theta} z_k \qquad (7)$$

where z_k is the phase center of the $k-th$ target.

As for the amplitude of the coherence, instead, the following model will be retained:

$$\gamma_{nm}^{(k)} = |\{\mathbf{R}_k\}_{nm}| = \rho_k^{-|b_n - b_m|\zeta} \tag{8}$$

where ρ_k will be referred to as decorrelation constant for the $k-th$ target and ζ is a normalizing constant such that the exponent in (8) is dimensionless. The role of the decorrelation constant is to describe in a simple fashion the loss of correlation due to the spatial structure of the $k-th$ target, avoiding the dependence upon a particular target model. Given the definition above, the decorrelation constant ranges from 0 to 1, corresponding to the cases of pure noise and of a perfectly coherent received signal (i.e. a point-like scatterer), respectively.

To sum up, after (7) and (8), model (2) is determined by a set of $N_x = 3K+1$ parameters, which will be denoted as $\mathbf{z}$, $\boldsymbol{\rho}$,$\boldsymbol{\sigma}$, where: $\mathbf{z}$ represents the K phase center locations; $\boldsymbol{\rho}$ represents the K decorrelation constants; $\boldsymbol{\sigma}$ represents the $K+1$ scattered powers. Furthermore, note that the number of targets within the resolution cell, K, is in general not known, and thus it must be inferred from the data.

B. Covariance Matching Estimation Technique (COMET)

In principle, the availability of a model for the covariance matrix suffices for solving for the unknowns through Maximum Likelihood (ML) estimation. This solution, however, would not be efficient, since it requires an exhaustive search in a parameter space with N_x dimensions.A significant complexity reduction may be achieved by applying the Extended Invariance Principle (EXIP), which allows to solve the problem by minimizing a weighted Frobenius norm of the difference between the sample covariance matrix and the model in (2) [13]. In formula:

$$\left(\widehat{\mathbf{z}}, \widehat{\boldsymbol{\rho}}, \widehat{\boldsymbol{\sigma}}; \widehat{K}\right) = \underset{\mathbf{z},\boldsymbol{\rho},\boldsymbol{\sigma},K}{\arg\min} \left\{ J^{(K)}\left(\mathbf{z}, \boldsymbol{\rho}, \boldsymbol{\sigma}\right) \right\} \tag{9}$$

where:

$$\begin{aligned} & J^{(K)}\left(\boldsymbol{\xi}, \boldsymbol{\rho}, \boldsymbol{\sigma}\right) \\ = \;& trace\left(\widehat{\mathbf{R}}^{-1}(\widehat{\mathbf{R}} - \mathbf{R})\widehat{\mathbf{R}}^{-1}(\widehat{\mathbf{R}} - \mathbf{R})\right) \end{aligned} \tag{10}$$

The role of the weighting matrix $\widehat{\mathbf{R}}^{-1}$is to provide the optimal set of weights to provide the asymptotical optimality of the estimates. This approach, known in literature as Covariance Matching Estimation Technique (COMET), has three major advantages: it may be applied even in the case of non-Gaussian distributions; it is asymptotically optimal in the case of a Gaussian distribution; the estimates of the polarimetric signatures are obtained in closed form. In this way, the dimension of the search space has been reduced to two unknowns per target.

III. Extension to multi polarimetric-and multi-baseline data

In the case where a single, multi polarimetric image is available, the element of diversity among the different scattering mechanisms is given by their polarimetric signature. Once again, this information may be embedded in the data covariance matrix. Letting $\mathbf{y}_{MP} = \left[\begin{array}{ccc} y_{HH} & \sqrt{2}y_{HV} & y_{VV} \end{array}\right]^T$ represent the stack of the multi polarimetric data[1] at a given location in the slant range, azimuth plane, and again under the assumption of statistical independence among different mechanisms, the data covariance matrix is given by:

$$\mathbf{C} = E\left[\mathbf{y}_{MP}\mathbf{y}_{MP}^H\right] = \sum_{k=1}^{K+1} \mathbf{C}_k \tag{11}$$

where $\mathbf{C}_k$, hereinafter referred to as polarimetric signature, is the single image, multi polarimetric covariance matrix of the data due to the *k-th* scattering mechanism. As in (2), the last term of the sum has been associated to white noise contributions.

A. A tomographic-polarimetric model

A straightforward way to provide a model for the covariance matrix of a multi-polarimetric, multi-baseline (MPMB) data is to force the hypothesis that the structure matrices do not vary across the polarimetric channels. This hypothesis is equivalent to expressing the covariance matrix of the MPMB through a sum of $K+1$ Kronecker products:

$$\mathbf{A} = E\left[\mathbf{y}\mathbf{y}^H\right] = \sum_{k=1}^{K+1} \mathbf{C}_k \otimes \mathbf{R}_k \tag{12}$$

where $\mathbf{y} = \left[\begin{array}{ccc} \mathbf{y}_{MB}^H(HH) & \sqrt{2}\mathbf{y}_{MB}^H(HV) & \mathbf{y}_{MB}^H(VV) \end{array}\right]^H$ is the stack of MPMB data.

The condition for the general validity of model (12) is that *some* parametrization (i.e.: some physical model) exists such that structure matrices are invariant with respect to the polarimetric channels. In the case of the parametrization adopted in Section II, this is equivalent to assuming that the phase center and the coherence loss due to spatial decorrelation associated to each scattering mechanism are invariant with respect to the choice of the polarimetric channel. This condition is verified for point-like targets, as those found in urban areas. For natural scenarios, instead, model (12) is to be intended as a reasonable approximation of the data covariance matrix, whereas there is not a rigorous physical evidence of its validity. From the numerical point of view, forcing model (12) allows not to raise excessively the number of the unknowns, limiting the computational burden and yielding more robust estimates. This model has also an advantage in terms of interpretation of the results, since it assigns a unique spatial distribution to each target within the resolution cell. Roughly speaking, this is equivalent to characterizing a forested area through its average spatial distribution across the three polarimetric channels, in such a way as to deal directly with the forest structure rather than with its electromagnetic properties. Furthermore, it is worthwhile noticing that model (12) is consistent with the two layered model exploited in single baseline PolInSAR [8] . Nevertheless, a separate tomographic analysis for each polarimetric channel can be performed as well, if need be.

[1]The VH channel has been neglected, by virtue of reciprocity.

B. MPMB COMET

Basing on (12), the COMET can be straightforwardly extended to the MPMB case as follows:

$$J\left(\mathbf{z},\boldsymbol{\rho},\{\mathbf{C}_k\}_{k=1}^{K+1};K\right)= \quad (13)$$
$$trace\left(\widehat{\mathbf{A}}^{-1}\left(\widehat{\mathbf{A}}-\mathbf{A}\right)\widehat{\mathbf{A}}^{-1}\left(\widehat{\mathbf{A}}-\mathbf{A}\right)\right)$$

where $\widehat{\mathbf{A}}$ is the sample estimate of $\mathbf{A}$ and $\{\mathbf{C}_k\}_{k=1}^{K+1}$ denote the set of the polarimetric signatures.

IV. Analysis of the Remningstorp forest site

This Section is devoted to reporting the results of the tomographic analysis of the forest site of Remningstorp, Sweden, on the basis of a data-set of $N = 9$ P-Band, fully polarimetric SAR images acquired by the DLR airborne system E-SAR in the framework of the ESA project BioSAR 2007. Prevailing tree species in the imaged scene are Norway spruce (Picea abies), Scots pine (Pinus sylvestris) and birch (Betula spp.). The dominant soil type is till with a field layer, when present, of blueberry (Vaccinium myrtillus) and narrow thinned grass (Deschampsia flexuosa). Tree heights are in the order of 20 m, with peaks up to30 m. The topography is fairly flat, terrain elevation above sea level ranging between 120 and 145 m. The acquisitions have been carried out from March to May 2007. The horizontal baseline spacing is approximately 10 m, resulting in a total horizontal baseline of approximately 80 m. The data has been motion-compensated, focused, and co-registered by DLR. The spatial resolution is approximately 2 m in the slant range direction and 1 m in the azimuth direction.

The top row of Fig. (1) shows an optical view of the Remningstorp test site captured from Google Earth, resampled onto the SAR slant range, azimuth coordinates, whereas the bottom row of the same figure shows the amplitude of the HH channel, averaged over the 9 images. Backscatter from open areas has turned out to be remarkably lower than that from forested areas (about 25 dB), as expected at longer wavelengths.

A. Preliminary analyses

In this section, a first qualitative discussion about the imaged scene is provided through the application of conventional and well assessed analysis techniques. The results here presented will serve as the basis for the validation of the outcomes of the tomographic analysis.

1) Amplitude stability analysis: An analysis of the amplitude stability of the data has been performed by computing the ratio μ/σ, where μ and σ denote the mean and the standard deviation of the amplitudes of the SLC images. The μ/σ index is widely used in Permanent Scatterers Interferometry (PSI) as a criterion to select the most coherent scatterers in the imaged scene [14]. As a result, for both the HH and VV channels the μ/σ index has resulted to be characterized by extremely high values ($\mu/\sigma > 15$), which indicates the presence of a highly stable scattering mechanism in the co-polar channels.

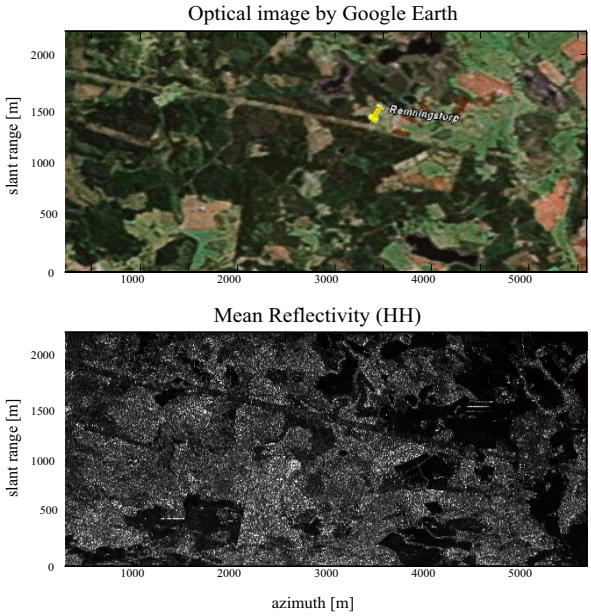

Fig. 1. Top row: Optical image of the Remningstorp forest site by Google Earth. Bottom row: Mean reflectivity of the HH channel.

2) Temporal decorrelation: Temporal decorrelation has been evaluated by exploiting the presence of additional zero baseline images. The temporal coherence at 56 days has been assessed in about $\gamma_{temp}^{HH} \simeq 0.85$ in the HH channel, $\gamma_{temp}^{VV} \simeq 0.8$ in the VV channel, and $\gamma_{temp}^{HV} \simeq 0.75$ in the HV channel, relatively to forested areas. Accordingly, the temporal stability of the scene is rather good for all the three polarimetric channels, indicating the presence of a stable scattering mechanism, especially in the co-polar channels.

3) Co-polar analysis: The information carried by the co-polar channels has been analyzed by averaging the backscattered powers and the co-polar interferograms (i.e.: the Hermitian product between the HH and VV channels) over all the 9 tracks and inside an estimation window as large as 50×50 square meters (ground range, azimuth). The distribution of the HH and VV total backscattered power with respect to the co-polar phase, $\Delta\varphi = \varphi_{HH} - \varphi_{VV}$, has shown to be substantially bimodal, high and low energy values being concentrated around $\Delta\varphi \approx 80°$ and $\Delta\varphi \approx 0°$, respectively, see Fig.(2). The coherence between the HH and VV channels has been assessed in about $\gamma_{copol} \approx 0.8$ in open areas and $\gamma_{copol} \approx 0.45$ in forested areas .

4) Non parametric Tomographic analysis: A first, non parametric, tomographic analysis has been carried out by evaluating the Capon spectra of the three polarimetric channels, see for example [2], [1], reported in Fig. (3). Each spectrum has been obtained by evaluating the sample covariance matrix at each range bin on the basis of an estimation window as large as 50×50 square meters (ground range, azimuth). The analyzed area corresponds to a stripe of the data along the

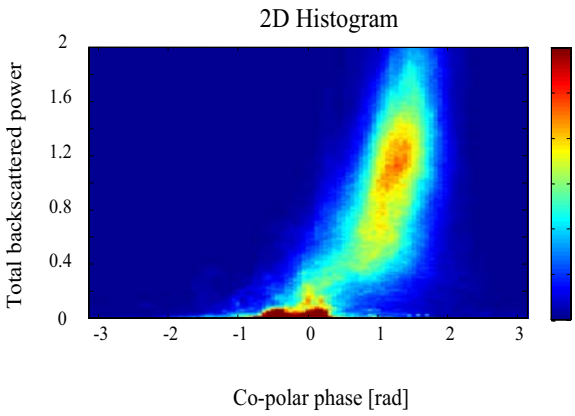

Fig. 2. Joint distribution of the total backscattered power and the co-polar phase for the co-polar channels. The total backscattered power has been obtained as the sum between the HH and VV backscattered powers. The color scale is proportional to the number of counts within each bin.

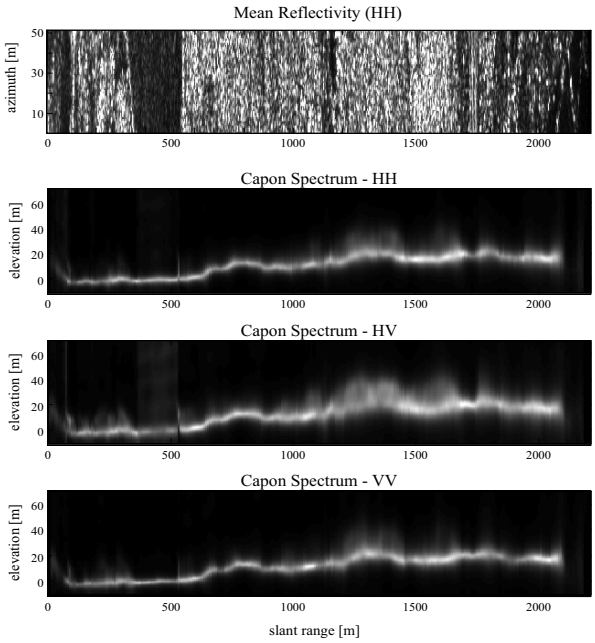

Fig. 3. Top panel: mean reflectivity of the data (HH channel) within a stripe as wide as 50 m in the azimuth direction. The underlying panels show the Capon Spectra for the three polarimetric channels. At every range bin the signal has been scaled in such a way as to have unitary energy.

slant range direction, shown in the top panel of Fig. (3). Almost the whole stripe is forested except for the dark areas in near range, corresponding to bare terrain. It may be observed that the spectrum is almost invariant to the choice of the polarimetric channel. Each spectrum is characterized by a narrow peak, above which a weak sidelobe is visible. As for the co-polar channels, this result is consistent with the hypothesis that a single scattering mechanism is dominant. It is then reasonable to relate such scattering mechanism to the double bounce contribution from trunk-ground and canopy-ground interactions, and hence the peak of the spectrum can be assumed to be located at ground level. The sidelobe above the main peak is more evident in the HV channel, but the contributions from ground level seem to be dominant as well, the main peak being located almost at the same position as in the co-polar channels. Accordingly, the presence of a relevant contribution from the ground has to be included in the HV channel too.

5) Preliminary discussion: Since the co-polar phase for both ground and canopy backscatter is expected to be null, [15], the value of $\Delta\varphi \approx 80°$ found in forested areas can only be interpreted as an index of the presence of a dihedral contribution. Now, whereas for a perfect conducting dihedral $\Delta\varphi$ is exactly $180°$, for a lossy dielectric dihedral a lower value of $\Delta\varphi$ is expected, due to the electromagnetic properties of the trunk-ground ensemble (in [16] for example, a co-polar phase of $94°$ has been observed for trunk-ground scattering). What makes the interpretation of the co-polar signature of forested areas not straightforward is that low values of the co-polar coherence have been observed, whereas dihedral contributions to the HH and VV channels are usually assumed to by highly correlated [15]. I see two possible explanations. The first one is that forested areas are characterized by an almost ideal dihedral scattering plus a significant contribution from canopy backscatter, which would explain both the low co-polar coherence and the reduction of $\Delta\varphi$ from the ideal value of $180°$ to $80°$. This interpretation, however, is not satisfying, since it is not consistent with the presence of highly amplitude stable targets nor with the Capon spectra in Fig. (3). At this point, a better explanation seems to be that to consider forested areas as being dominated by a *single* scattering mechanism, responsible for (most of) the coherence loss between the co-polar channels, highly coherent with respect to geometrical and temporal variations, and approximately located at ground level. From a physical point of view, it makes sense to relate such scattering mechanism to the ensemble of trunk-ground and canopy-ground interactions, eventually perturbed by the presence of understory, trunk and ground roughness, or by small oscillations in the local topography. It has to be remarked, however, that these results are peculiar to the Remningstorp test site, whereas in general a stronger contribution from canopy backscatter has been observed.

B. Model Based Tomography

The scene has been characterized as being constituted by two scattering mechanisms, plus a generic white noise term. Even though the temporal stability of the scene is rather good, especially in the HV channel the coherence loss due to temporal decorrelation is not negligible, and thus a brief discussion is required. In principle, temporal decorrelation could be properly handled by adding, at least, a further unknown for each target, in such a way as to estimate the coherence loss due to both the spatial structure and the temporal behavior of the targets. This solution, however, would complicate by far model inversion as for both the computational burden

and the conditioning of the problem, and hence I decided not to include temporal decorrelation in the model of the structure matrices. In support of this decision, it can be noted that it is sensible to retain that the redundancy provided by the availability of multi-baseline acquisitions can mitigate the impact of model mismatch due to temporal decorrelation with respect to the single baseline case. In particular, the optimal weighting matrix exploited in the figure of merit of the COMET, see (10), is based on the sample covariance matrix, and hence implicitly accounts for temporal decorrelation as well by associating lower weights to the interferometric pairs affected by temporal losses. Accordingly, T-SAR has been posed as the problem of estimating 13 unknowns, given by 2 target elevations, 2 decorrelation constants, and 9 scattered powers.

1) Elevation Estimates: The top row of Fig. (4) shows the map of the estimates relative ground elevation. The black areas correspond to area dominated by an unstructured scattering mechanism, as it is the case of lakes. The identification of such areas has been carried out after the analysis of the spatial decorrelation constant, as discussed hereinafter. The estimates relative to canopy elevation are visible in the bottom row of Fig. (4). In this case, the black areas have been identified by the algorithm as being characterized by the presence of (at most) a single target, which shows the effectiveness of the COMET in identifying bald and forested ares. It is worth noting the presence of a road, clearly visible in the optical image, see Fig. (1), crossing the scene along the direction from slant range, azimuth coordinates $(1850, 0)$ to $(1000, 5500)$. Along that road, a periodic series of small targets at an elevation of about 25 m have been found by the COMET. Since a power line passes above the road, it seems reasonable to relate such targets to the echoes from the equipment on the top of the poles of the power line. LIDAR measurements relative to ground and canopy elevation, provided by the Swedish Defence Research Agency (FOI), have been exploited as a validation tool [2]. As for ground elevation, a rather good agreement has been observed between T-SAR estimates and LIDAR measurements, the dispersion of the difference, $z_{SAR} - z_{LIDAR}$, being assessed less than 1 m, see Fig. (5). The result relative to canopy elevation is not that brilliant as the one relative to ground elevation, see the right panel of Fig. (5). This discrepancy is clearly imputable to the fact that the estimates yielded by T-SAR are relative to average the phase center elevation inside the estimation window, whereas LIDAR is only sensitive to the top height of the canopy. In particular, it is interesting to note that the canopy elevation provided by T-SAR appears to be slightly under-estimated with respect to LIDAR measurements, as a result of the under foliage penetration capabilities of P-band

[2]Canopy elevation has been extracted from the LIDAR measurements according to the following processing. First, an adaptive spatial smoothing has been performed, such that every sample of the processed map represented the average canopy layer elevation within the same 50×50 square meters window exploited in the tomographic analysis, having care to include in the computation only those samples where a return from the canopy was actually present. Then, a re-sampling operation has been performed to code the processed map onto SAR coordinates.

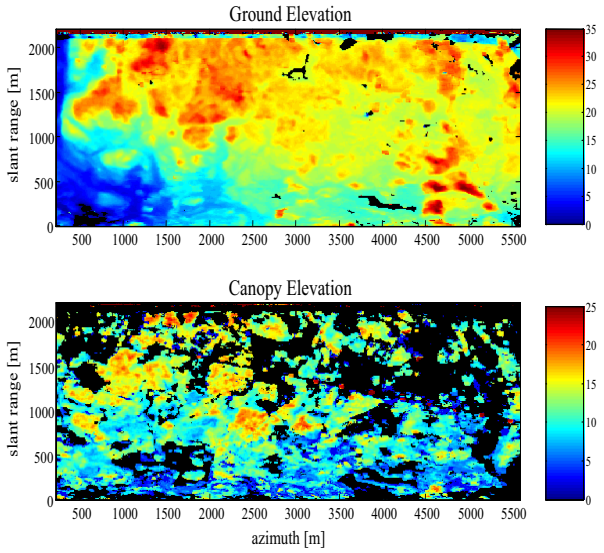

Fig. 4. Top row: estimated ground elevation. Black areas correspond to an unstructured scattering mechanism. Bottom row: estimated canopy elevation. Black areas correspond to absence of canopy.

microwaves. Nevertheless, the overall agreement between T-SAR and LIDAR is satisfactory, as shown by Fig. (6).

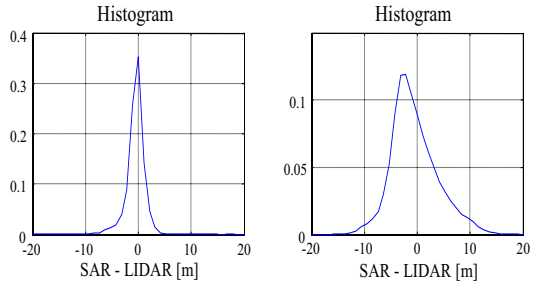

Fig. 5. Histograms of the differences of the elevation estimates relative to the ground and the canopy yielded by T-SAR and LIDAR measurements.

2) Estimates of the polarimetric signatures: Figure (7) reports the ratios between the estimated backscattered powers from the ground and the canopy (G/C ratio), for each polarimetric channel. As expected, in the co-polar channels the scattered power from the ground is significantly larger than canopy backscatter, the G/C ratio being assessed in about 10 dB. In the HV channel the scattered powers from the ground and the canopy are closer to each other even though ground contributions still appear to be dominant, resulting in a ground to canopy ratio of about 3 dB. It is interesting to note that the G/C of the HV channel has shown a good sensitivity with respect to the tree species, resulting in about 0 dB for pine stands and 8 dB for spruce stands.

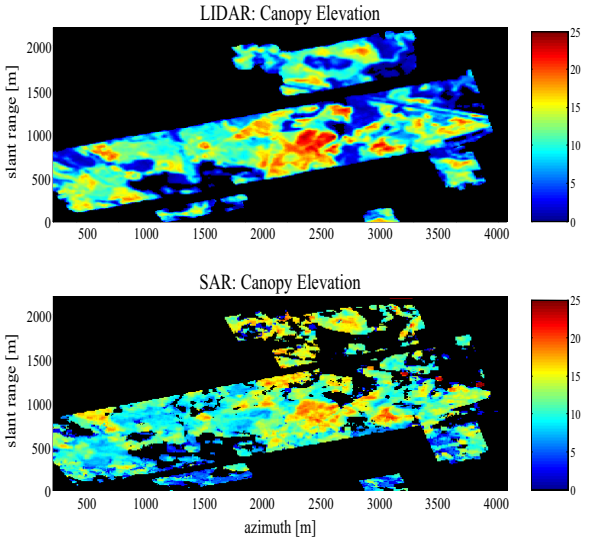

Fig. 6. Top row: canopy elevation estimated by LIDAR. Bottom row: canopy elevation estimated by T-SAR.

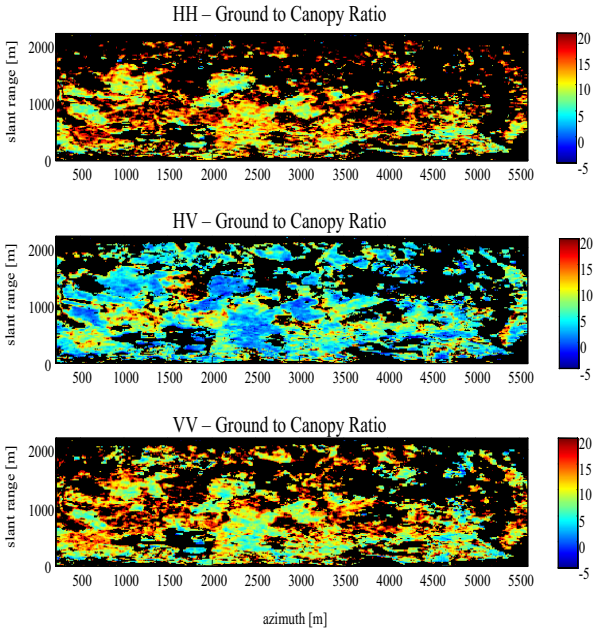

Fig. 7. Ground to Canopy Ratio for the three polarimetric channels.

C. Single Channel Tomographies

This Section is dedicated to reporting the results relative to the elevation estimates provided by processing the HH and the HV channel separately, compared to estimates yielded by the fully polarimetric (FP) tomography. The joint distributions of the elevation estimates yielded by the FP tomography and by the HH and HV tomographies are reported in Fig. (8). The results relative to the VV channel, not reported here, have been observed to be quite similar to those relative to the HH channel. It can be appreciated that, as expected, ground elevation is better estimated by processing the HH channel, whereas canopy elevation is better estimated by processing the HV channel. In all cases, however, the estimates are close to those provided by the FP tomography, proving that the tomographic characterization of forested areas may be carried out on the basis of a single polarimetric channel, provided that a sufficient number of acquisitions is available.

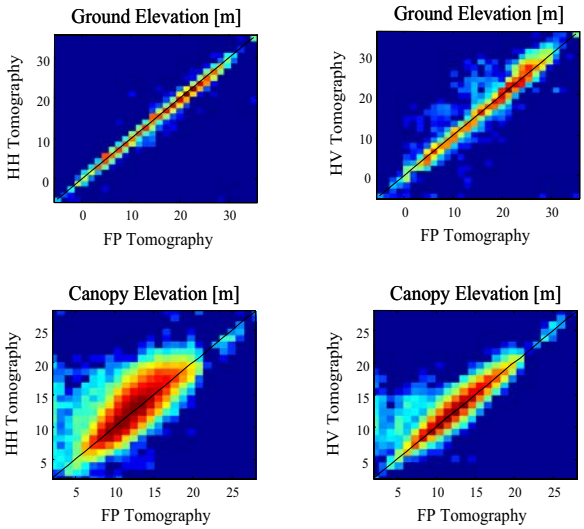

Fig. 8. Joint distribution of the elevation estimates yielded by processing the single channels separately (vertical axis) and by the best tomography (horizontal axis). The black line denote the ideal linear trend. The color scale is proportional to the natural logarithm of the number of counts within each bin.

D. 6 MHz Tomography

In order to provide an experimental discussions of the effects of pulse bandwidth, the data has been filtered in such a way as to reduce the bandwidth to 6 MHz (4 MHz at ± 3 dB), corresponding to a slant range resolution of about 30 m. As expected, reducing the signal bandwidth has resulted in an increased dispersion of the estimates. Nevertheless, results show that 6 MHz Tomography is possible.

V. Discussion and Conclusions

This paper has focused on the model based SAR tomographic techniques for the analysis of forested areas. Basing on a physical model of radar backscattering from forested areas, T-SAR has been posed in terms of a parametric estimation problem, that has been solved by exploiting statistical techniques. It has been shown, in particular, that the COMET provides a cost effective, asymptotically optimal strategy to perform model inversion basing on either single or multi polarimetric acquisitions. Moreover, it has been shown that the retrieval of the vertical structure of forested areas may be carried out on the basis of a single polarimetric channel as well

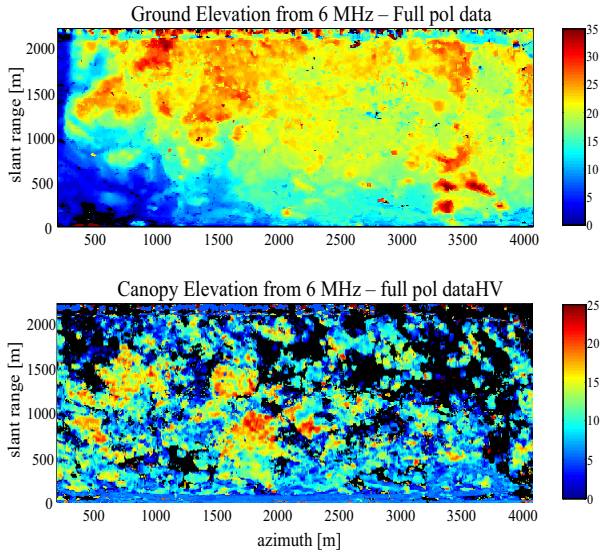

Fig. 9. Top row: estimated ground elevation. Black areas correspond to an unstructured scattering mechanism. Bottom row: estimated canopy elevation. Black areas correspond to absence of canopy.

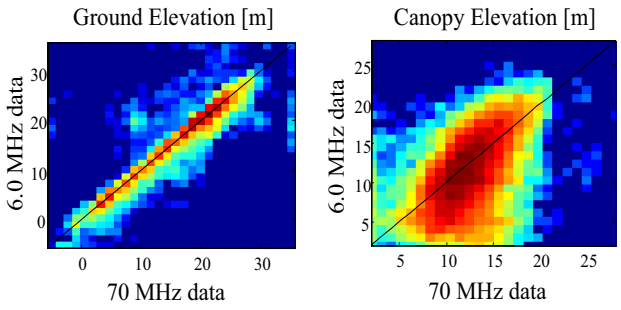

Fig. 10. Joint distribution of the elevation estimates yielded by processing the 6 MHz data (vertical axis) and by the best tomography (horizontal axis). The black line denote the ideal linear trend. The color scale is proportional to the natural logarithm of the number of counts within each bin.

as basing on a 6 MHz data. All the results that have been obtained have been shown to be consistent with those obtained by applying non tomographic or non model based techniques. All these arguments seem to confirm the validity of modeling the scene as the superposition of two decorrelating targets. From the physical point of view, this result is probably due to the sparsity of the vegetation that characterizes the Remningstorp forest site, and to the usage of a P-Band sensor. In general, however, the choice of a physical model is expected to depend heavily on the kind of forest under analysis. Moving to the results relative to the Remningstorp site, many experimental evidences have been provided that indicate that not only in the co-polar channel, but also in the HV the contribution from the ground dominate that from the canopy. Such result has been obtained qualitatively by evaluating the Capon Spectra, and quantitatively through estimation of the backscattered powers. Such result indicates that not only canopy-ground interactions, but also trunk-ground interactions have to be accounted for in modeling backscattering in the HV channel.

VI. Acknowledgment

I would like to acknowledge insights and valuable discussions with Prof. Fabio Rocca and Prof. Andrea Monti Guarnieri, at Politecnico di Milano. I would also like to thank to Dr. Malcom Davidson (ESA), Dr. Irena Hajnsek (DLR), Dr. Kostas Papathanassiou (DLR), Dr. Fabrizio Lombardini (Università di Pisa), and Prof. Lars Ulander (FOI), with whom I could discuss many of the results within this paper.

References

[1] F. Lombardini and A. Reigber, "Adaptive spectral estimation for multi-baseline sar tomography with airborne l-band data," *Geoscience and Remote Sensing Symposium, 2003. IGARSS '03. Proceedings. 2003 IEEE International*, vol. 3, pp. 2014–2016, July 2003.

[2] F. Gini, F. Lombardini, and M. Montanari, "Layover solution in multi-baseline sar interferometry," *Aerospace and Electronic Systems, IEEE Transactions on*, vol. 38, no. 4, pp. 1344–1356, Oct 2002.

[3] S. Sauer, L. Ferro-Famil, A. Reigber, and E. Pottier, "Multibaseline pol-insar analysis of urban scenes for 3d modeling and physical feature retrieval at l-band," *Geoscience and Remote Sensing Symposium, 2007. IGARSS 2007. IEEE International*, pp. 1098–1101, 23-28 July 2007.

[4] G. Fornaro, F. Lombardini, and F. Serafino, "Three-dimensional multipass sar focusing: experiments with long-term spaceborne data," *Geoscience and Remote Sensing, IEEE Transactions on*, vol. 43, no. 4, pp. 702–714, April 2005.

[5] S. R. Cloude, "Dual-baseline coherence tomography," *Geoscience and Remote Sensing Letters, IEEE*, vol. 4, no. 1, pp. 127–131, Jan. 2007.

[6] ——, "Multifrequency 3d imaging of tropical forest using polarization coherence tomography," in *Eusar 2008*, 2008.

[7] S. Cloude and K. Papathanassiou, "Polarimetric sar interferometry," *Geoscience and Remote Sensing, IEEE Transactions on*, vol. 36, no. 5, pp. 1551–1565, Sep 1998.

[8] K. Papathanassiou and S. Cloude, "Single-baseline polarimetric sar interferometry," *Geoscience and Remote Sensing, IEEE Transactions on*, vol. 39, no. 11, pp. 2352–2363, Nov 2001.

[9] S. Durden, J. van Zyl, and H. Zebker, "Modeling and observation of the radar polarization signature of forested areas," *Geoscience and Remote Sensing, IEEE Transactions on*, vol. 27, no. 3, pp. 290–301, May 1989.

[10] R. Bamler and P. Hartl, "Synthetic aperture radar interferometry," *Inverse Problems*, vol. 14, pp. R1–R54, 1998.

[11] H. A. Zebker and J. Villasenor, "Decorrelation in interferometric radar echoes," *IEEE Transactions on Geoscience and Remote Sensing*, vol. 30, no. 5, pp. 950–959, sept 1992.

[12] F. Gatelli, A. Monti Guarnieri, F. Parizzi, P. Pasquali, C. Prati, and F. Rocca, "The wavenumber shift in SAR interferometry," *IEEE Transactions on Geoscience and Remote Sensing*, vol. 32, no. 4, pp. 855–865, July 1994. [Online]. Available: http://www.elet.polimi.it/upload/monti/papers/gatelli94.pdf

[13] B. Ottersten, P. Stoica, and R. Roy, "Covariance matching estimation techniques for array signal processing applications," *Digital Signal Processing*, vol. 8, no. 3, pp. 185–210, July 1998.

[14] A. Ferretti, C. Prati, and F. Rocca, "Permanent scatterers in SAR interferometry," *IEEE Transactions on Geoscience and Remote Sensing*, vol. 39, no. 1, pp. 8–20, Jan. 2001.

[15] A. Freeman and S. Durden, "A three-component scattering model for polarimetric sar data," *Geoscience and Remote Sensing, IEEE Transactions on*, vol. 36, no. 3, pp. 963–973, May 1998.

[16] D. R. Sheen, N. L. VandenBerg, S. J. Shackman, D. L. Wiseman, L. P. Elenbogen, and R. F. Rawson, "P-3 ultra-wideband SAR: Description and examples," *IEEE AES Systems Magazine*, pp. 25–29, Nov. 1996.